

Single-Cell Redox Metabolism

Plasmonic Nanoparticle Monolayer-Decorated Nanopipette Enabling in Situ Monitoring of Single-Cell Redox Metabolism

Lei Jiang⁺, Mengqi Zhao⁺, Hanbin Xu, Xin Ding, Qiaoyi Lu, Jiwei Liu, Liping Song, Lijuan Gong, Dawei Li,^{*} and Youju Huang^{*}

Abstract: The in-depth study of how single cells respond to redox perturbations is pivotal for predicting cell fate decisions. Surface-enhanced Raman spectroscopy (SERS)-active nanopipettes hold promise for single-cell analysis, yet challenges remain in achieving both signal sensitivity and reproducibility. Here, a plasmonic nanoparticle monolayer-decorated nanopipette has been developed, which serves as a biomimetic endoscope to monitor single-cell redox metabolism. This is accomplished by the conformal transferring of gold nanoparticle monolayer onto the nanopipette followed by the functionalization of redox-responsive probes. The strong near-field coupling within monolayer forms uniform hotspots, enabling highly sensitive and reproducible tracking of SERS signals changes triggered by redox species. Modulated by the nanopipette technology, the endoscope allows for in situ monitoring of global redox states with low invasiveness and high spatial resolution. Further, study of ferroptosis events via simultaneous optical and electrical recording elucidates the correlation between redox imbalance and membrane damage during various ferroptosis-inducers stimulation, which has not been observed at the single-cell level. This work provides profound insights into the cellular redox dynamics, contributing to a deeper understanding of related physiopathological pathways.

Introduction

Redox homeostasis is key to the adaptation of cellular processes such as the cell cycle, apoptosis events, and immune response.^[1,2] Abnormal redox metabolism is linked to conditions like cardiovascular diseases, liver damage, and cancer.^[3,4] The study of single-cell redox metabolism could offer a deep insight into cellular heterogeneity with respect to different perturbations, which helps forecast cellular fate decisions and diseases progression.^[5,6] A real-time quantitative single-cell detection method is thus critical for tracking and cataloging the heterogeneity, as well as understanding the mechanisms of these regulatory processes. The use of

fluorescent dyes meets the requirements with high spatial resolution, but tends to interrupt cellular activities, difficult to comprehensively evaluate global redox status. In terms of some noninvasive techniques such as nanoelectrochemical analysis, complicated intracellular environment may cause a certain signal interference.^[7-9]

Surface/Tip-enhanced Raman spectroscopy (SERS/TERS), known for its high specificity, antiinterference ability, and minimal invasiveness, is a robust bioanalytical technique capable of probing spatiotemporal information of single living cells.^[10-14] As for the direct application of colloidal nanomaterials, their uncontrollable aggregation, long incubation time (30 min to 2 h), and possible cytotoxicity present concerns for the accuracy of single-cell analysis. Although TERS allows nondestructive chemical characterization of cells at the nanoscale, it is technically challenging because of meticulous preparation of TERS probe and biological samples.^[15,16] Comparatively, SERS-active nanopipettes offer flexible tools for single-entity analysis, meanwhile maintaining the real-time response, minimal damage, and high spatial resolution.^[17-20]

Considering typical redox indicators like reactive oxygen species (ROS) and glutathione present in individual cells at extremely low and heterogeneous concentrations, it is necessary to design highly sensitive SERS-active nanopipettes in a reproducible and controllable manner. Electrostatic assembly is capable of positioning diverse nanoparticles (NPs) and tailoring NPs density on nanopipettes surface.^[21,22] For example, Masson et al. used a block copolymer brush-layer film as the electrostatic adsorption template to yield a homogeneous deposition of gold nanoparticles (AuNPs).^[23-26] However, inconsistent electrostatic field due to the nanometer size and

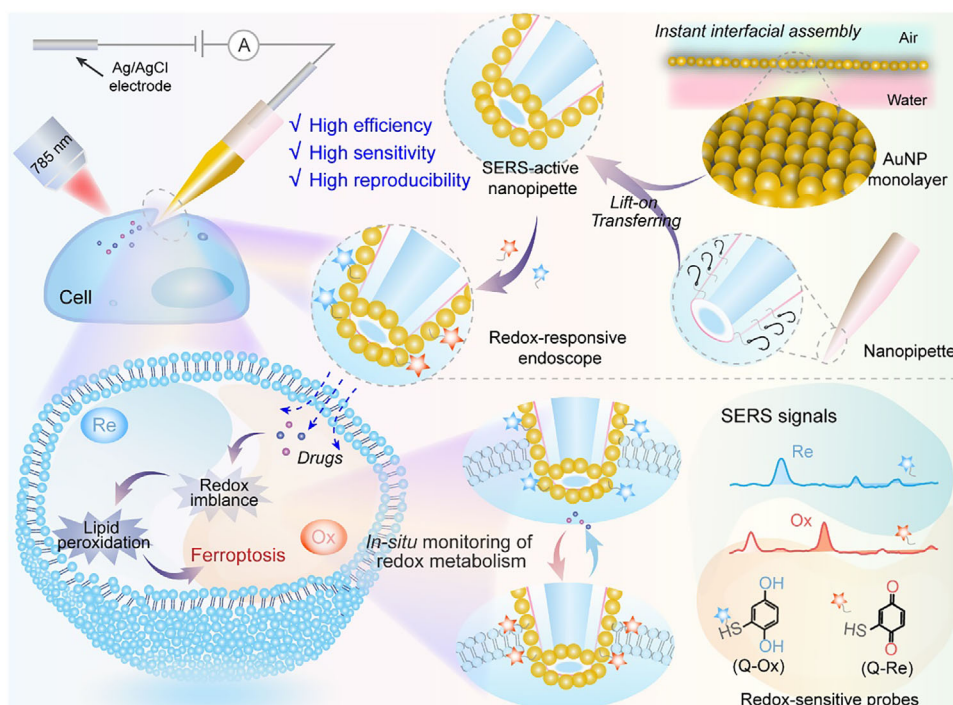
[*] Dr. L. Jiang⁺, X. Ding, Q. Lu, J. Liu, Dr. L. Song, Prof. Y. Huang
College of Material, Chemistry and Chemical Engineering, Key
Laboratory of Organosilicon Chemistry and Material Technology,
Ministry of Education, Hangzhou Normal University, Hangzhou,
Zhejiang 311121, P.R. China
E-mail: yjhuang@hznu.edu.cn

M. Zhao⁺, H. Xu, L. Gong, Prof. D. Li
Center for Materiobiology & Dynamic Chemistry, School of
Chemistry & Molecular Engineering, East China University of
Science and Technology, Shanghai 200237, P.R. China
E-mail: dawei@ecust.edu.cn

Dr. L. Jiang⁺
Hunan Provincial Key Laboratory of Micro & Nano Materials
Interface Science, College of Chemistry & Chemical Engineering,
Central South University, Changsha, Hunan 410083, P.R. China

[⁺] Both the authors contributed equally to this work.

 Additional supporting information can be found online in the
Supporting Information section



Scheme 1. Representation of the concept of AuNP monolayer-decorated nanopipette to in situ monitor redox metabolism at single-cell level. Re and Ox represent the reduction and oxidation.

the high-curvature variation of the tip hampers controllable assembly of charged NPs with dense coating and narrow nanogap. Other methods, such as chemical deposition and magnetron sputtering, are either time-consuming or difficult to rationally tailor the NPs size and distribution, which are detrimental to the sensing performance.^[27,28] Consequently, precise assembling and positioning a large amount of NPs on nanotips in a reproductive way still remains challenging.

Based on the previous researches, we turned our attention to uniform metallic NPs films that exhibit strong electromagnetic fields coupling. Our group recently developed different techniques for constructing macroscopic and uniform NPs films and exploited their potential in sensing applications.^[29–31] One of them known as instant interfacial assembly is able to quickly (~ 5 s) form the NPs monolayer with large area, high density, and narrow nanogap. Followed by a conformal lift-on transferring, such assembled monolayer can be delivered onto different substrates in a nondestructive manner.^[31] Accordingly, the combination of well-designed monolayer with nanopipettes decoration may serve as an effective pathway to address conundrums faced by conventional methods.

Therefore, a plasmonic nanoparticle monolayer-decorated nanopipette has been developed in this work, which can realize in situ monitoring of single-cell redox metabolism. Our strategy involves transferring a compact AuNP monolayer onto the nanopipette surface, followed by modifying redox-sensitive probes, 2-mercaptobenzoquinone (Q-Ox) or 2-mercaptohydroquinone (Q-Re) (Scheme 1). As compared to conventional methods, this design can offer narrower nanogaps and a richer distribution of hotspots, which

improves the sensitivity of SERS detection. By integrating a high-precision nano-positioning system, the endoscope enables real-time monitoring of the global redox status in single living cells with minimal invasiveness and high spatial resolution. Furthermore, aided by nanopipette-based electrical measurements, we conduct the single-cell ferroptosis study via the endoscope to better understand the correlation between redox imbalance and membrane damage induced by ferroptosis inducers, a relationship that has yet to be explored at the single-cell level. This strategy, incorporating NP monolayer and nanopipette technology, proves to be powerful for dynamic analysis of cellular behaviors.

Results and Discussion

Fabrication and Characterization of the Redox-Sensitive Endoscope

A highly SERS-active nanopipette was first prepared by dense decoration of plasmonic AuNP monolayer on nanotips surface. Prior to the decoration, AuNPs with high uniformity in both morphology and size (~ 45 nm, Figure S1) were synthesized to form AuNP monolayer through the perfluorodecanethiol (PFT)-mediated instant interfacial assembly.^[31] Figure 1a demonstrates that a macroscopic monolayer was obtained by PFT-induced assembly, which presented single-storied and dense NPs arrangement. The monolayer was further characterized by high resolution transmission electron microscope (HRTEM), grazing-incidence small-angle X-ray scattering (GISAXS), and ultraviolet-visible (UV-vis)

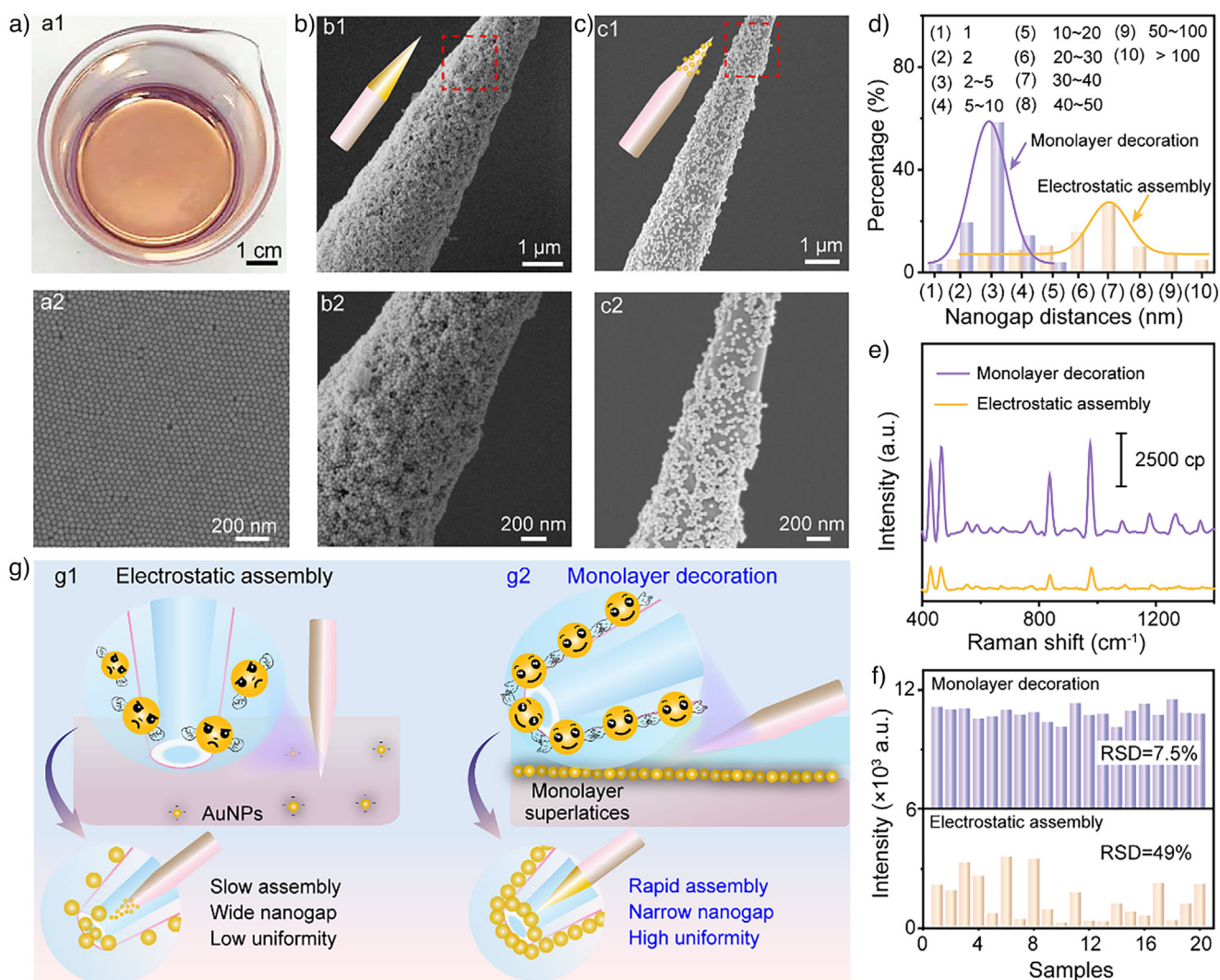


Figure 1. Comparison of SERS performance of nanopipettes fabricated by the electrostatic assembly and monolayer decoration. a-a1) The optical image of a macroscopic AuNP monolayer, (a-a2) The SEM image of AuNP monolayer. b-b1) The SEM image of monolayers-decorated nanopipette. (b-b2) The enlarged view in the red rectangle in b-b1. c-c1) The SEM image of electrostatically assembled-nanopipette, (c-c2) The enlarged view in the red rectangle in c-c1. d) Statistical distributions of nanogap distances were obtained by measuring 200 gaps. e) The average SERS spectra of Q-Re and f) SERS intensity of the peak at 476 cm⁻¹ acquired from the tip of 20 nanopipettes. Top: Monolayer decoration; Bottom: Electrostatic assembly. g) Schematics of the (g1) electrostatic assembly and (g2) monolayer decoration.

absorption measurements (Figure S2), revealing a highly uniform microstructure with the interparticle spacing of 2.5 ± 2.1 nm. Subsequently, using the conformal lift-on transferring technology, the monolayers were systematically transferred to the bare glass nanopipette possessing tip with a diameter of ca. 150 nm (Figures 1b and S3). Meanwhile, we compared this strategy with the electrostatic interaction-based assembly, one of the most commonly used methods (Figure S4).^[32,33] As shown in Figure S5A, a monolayer formed a close-packed highly ordered array on the nanopipette surface with the particle density as 2600 counts μm^{-2} . Moreover, a narrower nanogap distribution ranging from 2 to 5 nm can be observed (Figure 1d), as compared to that generated by the electrostatic assembly with the NPs distance from 5 to 50 nm and the density as 1060 counts μm^{-2} (Figures c,d, and S5B). Unlike time-

consuming electrostatic assembly (>6 h), the described approach showed a superior efficiency with a much shorter time (~ 5 min). In addition, taking Q-Re as the model molecule, its signal intensity obtained from monolayer-decorated nanopipettes was enhanced 5.5-fold than electrostatic assembly ones (Figures 1e and S6). This is mainly ascribed to the large particle density and narrow nanogaps that yielded abundant hotspots, facilitating strong electromagnetic enhancement, desirable for sensitive measurements. Furthermore, the relative standard deviation (RSD) of SERS intensities acquired from monolayer-decorated nanopipettes was as low as 7.5% ($n = 20$), much lower than that of electrostatic assembly (RSD = 49%, Figure 1f). Taken together, the monolayer decoration-based method showed desirable advantages in aspects of decoration efficiency, SERS activity, and signal reproducibility (Figure 1g),

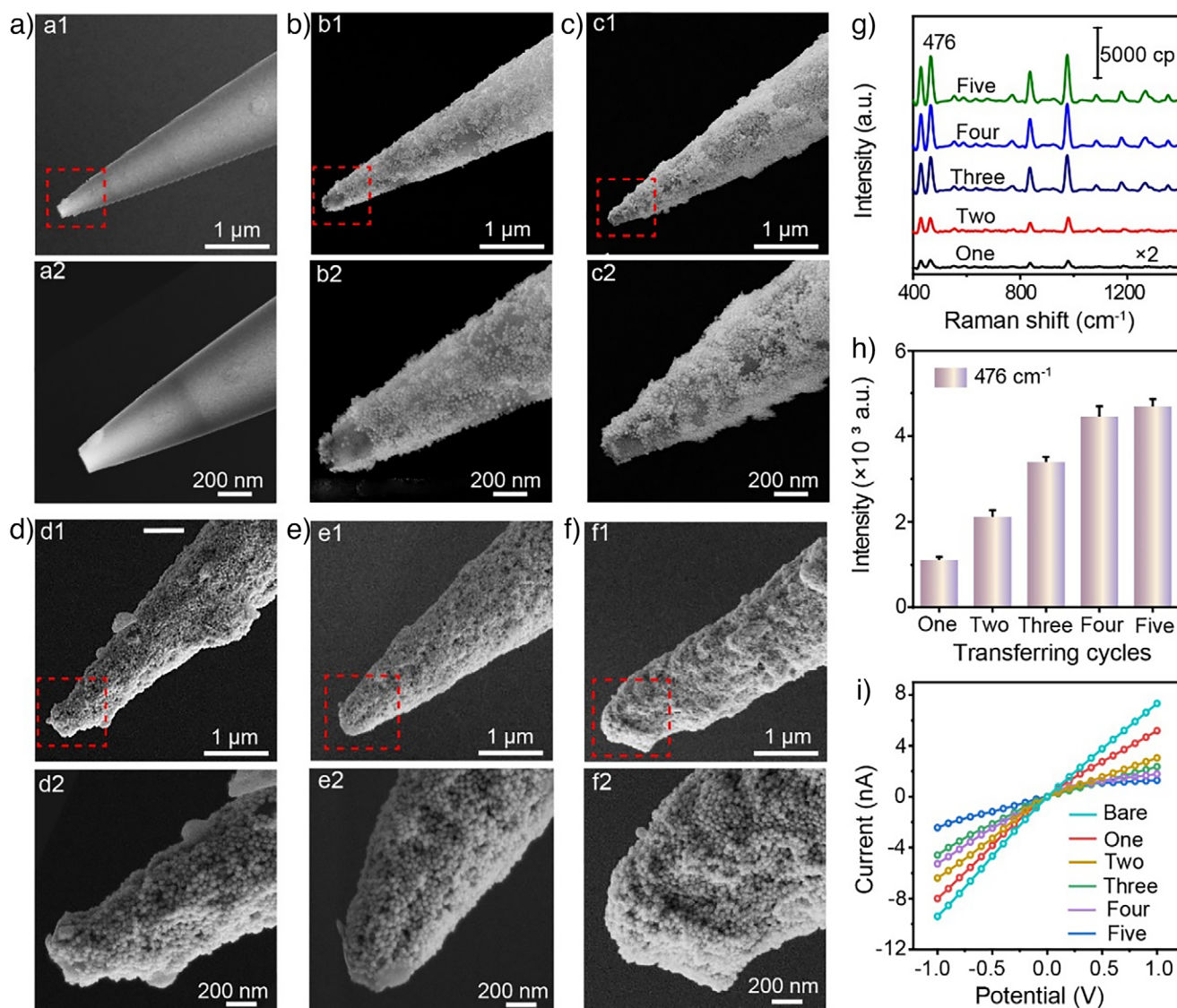


Figure 2. SEM images of monolayer-decorated nanopipettes obtained by different transferring cycles, a) bare, b) one, c) two, d) three, e) four and f) five cycles. a2, b2, c2, d2, e2, and f2 correspond to the enlarged image view in the red rectangle in a1, b1, c1, d1, e1, and f1 respectively. g) and h) The comparison of SERS effects. i) Stepwise I-V responses of the nanopipettes decoration. Supporting electrolyte was 2 mM phosphate buffered saline (PBS). Data with error bars present the mean \pm standard deviation (SD) of independent replicates ($n = 3$).

indicating a high potential for quantitative and sensitive analysis.

Moreover, we found that the thickness of NPs films was a critical factor affecting the performance of single-cell SERS measurement. Figure 2a–f shows the scanning electron microscope (SEM) images of bare and plasmonic NP monolayer-decorated nanopipettes obtained by increasing the transferring cycles from one to five. As shown, the NP film on nanopipettes surface became more continuous, and the coverage nearly increased to 100% when the cycle reached three (Figure 2d). The nanopipettes after NP monolayer decoration remained a conformal shape, and their orifice sizes could be systematically controlled from 210 ± 25 nm to 625 ± 42 nm with the accumulation of AuNPs at the tip (Figures S7–S11 and Table S1). SERS mapping of tips using the peak at 476 cm^{-1} indicated a 4.8-

fold increase with the transferring extended to five cycles (Figure 2g,h). In addition, no significant variation in the SERS performance was observed under the same transferring cycles (Figure S12). The SERS enhancement factors corresponding to different transferring cycles were estimated to be about $0.13\text{--}6.30 \times 10^6$ (Figure S13 and Table S2, see details in Supporting Information). Considering the trade-off between SERS effects and appropriate tip size for single cell analysis, we chose four cycles to conduct lift-on transferring. Besides, the current–voltage (I–V) curves showed negatively rectified and permselective transport of ions (Figure 2i), which indicated the tips of all resulting nanopipettes remained open, allowing for electroosmosis modulation.^[34] Once the decoration completed, the redox-responsive endoscope was obtained by modifying Q-Re (or Q-Ox) molecules with the optimal concentration and modification time (Figure S14)

to read out the spectroscopic changes possibly triggered by redox species.

Feasibility Study for Probing Redox Changes in Solution

Since cellular redox environment is mainly balanced by oxidative and reductive species,^[1,4] they were treated as significant indicators to monitor redox changes using the endoscope on the basis of the proposed pathways (Figures 3a and S15). As depicted in Figures 3b and S16, SERS spectra of the endoscope (modified with reduction-sensitive Q-Re) changed significantly in the presence of typical reductive species (glutathione (GSH), cysteine (Cys), and ascorbic acid (AA)). The characteristic peak of reduced Q-Re can be observed at 900 cm^{-1} (indexed to $\nu_s\text{ C-O} + \nu_s\text{ CCC}$)^[35] during the process of reaction with AA, GSH, and Cys, indicating the formation of Q-Ox. Meanwhile, the peak at 476 cm^{-1} assigned to $\nu_s\text{ CCC}$ kept unchanged (Figure S17 and Table S3). It thus could be as an inner reference for built-in correction. Figure 3b shows that the intensity of 900 cm^{-1} (I_{900}) increased with time going by. As a result, we constructed an individual plot of the ratio of I_{900} to I_{476} (I_{900}/I_{476}) as a function of time. The ratio increased quickly in the first 5 min in a similar fashion for AA, GSH, and Cys (Figure 3c), which indicated that the endoscope could respond to reduction state rapidly. Further, evaluation of the kinetic behaviors revealed the pseudo first-order reaction with different rate constants (k), i.e., $k_{\text{AA}} > k_{\text{GSH}} > k_{\text{Cys}}$ (Figure S17D), consistent with the variation of reductive activity of them.^[36] Furthermore, good linear relationships were found between I_{900}/I_{476} and the concentrations of reductive species (Figure 3e,f, and S18). The limits of detection (LODs) for AA, GSH, and Cys were determined to be 18.1, 125.3, and 566.7 nM (3σ).

Inspired by the redox-activity and reversible structural transformation of quinone/hydroquinone moieties, we also investigated reaction kinetics of the reduced endoscope responding to oxidative species (hydrogen peroxide (H_2O_2), hydroxyl radical ($\cdot\text{OH}$), and hypochlorous acid (HClO)). As shown in Figures 3b and S19, the characteristic peak at 982 cm^{-1} (assigned to $\nu_s\text{ C=O} + \nu_s\text{ CCC}$)^[35] sharply rose after addition of those species. I_{982} under different conditions reached a plateau within 5 min (Figure 3d), indicating that the endoscope could detect them efficiently and rapidly. Similarly, the oxidation reactions followed the principle of the pseudo first-order kinetic behavior, with an order of rate constants $k_{\cdot\text{OH}} > k_{\text{HClO}} > k_{\text{H}_2\text{O}_2}$. LODs for $\cdot\text{OH}$, HClO, and H_2O_2 were calculated to be 5.8, 31.2, and 68.7 nM (Figures 3g and S20). As compared to recently reported redox sensing techniques (Table S4), the endoscope possessed a superior capability of broadly detecting redox species with high efficiency and sufficient sensitivity as required by the single-cell analysis. Moreover, no distinguishable SERS spectra change was observed after storage in fresh cell lysate for >48 h, indicating the long-term stability for biosensing in living cells (Figure S21A). Further, stability testing conducted in the physiological pH range (5.5 – 8.0) also demonstrated the reliability for probing the redox changes in biological environments (Figure S21B).

In Situ SERS and Electrical Measurements in Single Cells

Accordingly, the proposed endoscope would be ideal for comprehensively evaluating intracellular redox homeostasis. Coupled with the highly precise nano-positioning system and patch clamp amplifier, a home-built experimental setup for simultaneous SERS and electrical recording was established (Figure 4a). The typical current versus time curve in Figure S22 indicated the successful application to the single cell, without damaging the integrity of cell membrane (Figure 4b and S23). The insertion of the endoscope was not sufficiently traumatic to the cells to trigger a substantial oxidative stress response (Figure 4d and S24). Furthermore, the calcein acetoxyethyl ester/propidium iodide (calcein-AM/PI) staining proved the cell viability after the living cells were penetrated by the nanotips even experiencing a long duration of 90 min (Figure S25). These clearly demonstrate a favorable feasibility of the endoscope to support dynamic single-cell monitoring with low-invasiveness.

In view of sufficient availability of tumor-relevant GSH and ROS, which play crucial roles in redox signaling and homeostasis,^[37,38] we systematically investigated whether the endoscope could monitor real-time changes of their contents (Figure 4d). N-ethyl maleimide (NEM), a well-known thiol scavenger,^[39] was introduced and living cells were analyzed over time. As expected, GSH depletion generated significant decrease of reduction channel (I_{900}) relative to the control group (Figure S26). The quantification based on I_{900}/I_{476} showed approximate 2.1-fold fall after NEM stimulation lasting for 5 min, whereas the oxidation channel I_{982}/I_{476} was gradually enhanced (Figure 4e,f). After 30 min, the concentrations of GSH and ROS were nearly restored to levels before NEM treatment, ascribing to the delayed supplementation of GSH.^[40] Correspondingly, the deficiency of GSH led to the accumulation of ROS provisionally, further demonstrating the mutual interactions between them in cells. Moreover, the RSDs of I_{900}/I_{476} and I_{982}/I_{476} from these cells recorded at each time point varied between 14–21% ($n = 8$), larger than the deviation of the measurement in solution (9.7%, $n = 8$), which was mainly due to the natural variability of single cells. These results preliminarily indicate that the endoscope is promising for in situ and dynamic monitoring of global redox states in single cells.

Real-Time Monitoring of Redox Changes in Ferroptosis Events

Ferroptosis, a type of nonapoptotic and iron-dependent cell death, involves in lipid peroxidation together with oxidative stress and the loss of plasma membrane integrity.^[41] Recent studies have focused on inducing ferroptosis for cancer treatment using specific drugs that alter cellular redox environment.^[42] Clarifying and comparing drugs effect on intracellular redox metabolism is of great importance.

Encouraged by the capability of simultaneous optical and electrical recording, we determined the redox changes in response to different ferroptosis inducers using the endoscope. Before the insertion of the endoscope, we first recorded continuous current versus time traces to analyze

a) Redox-responsive measurements in solution

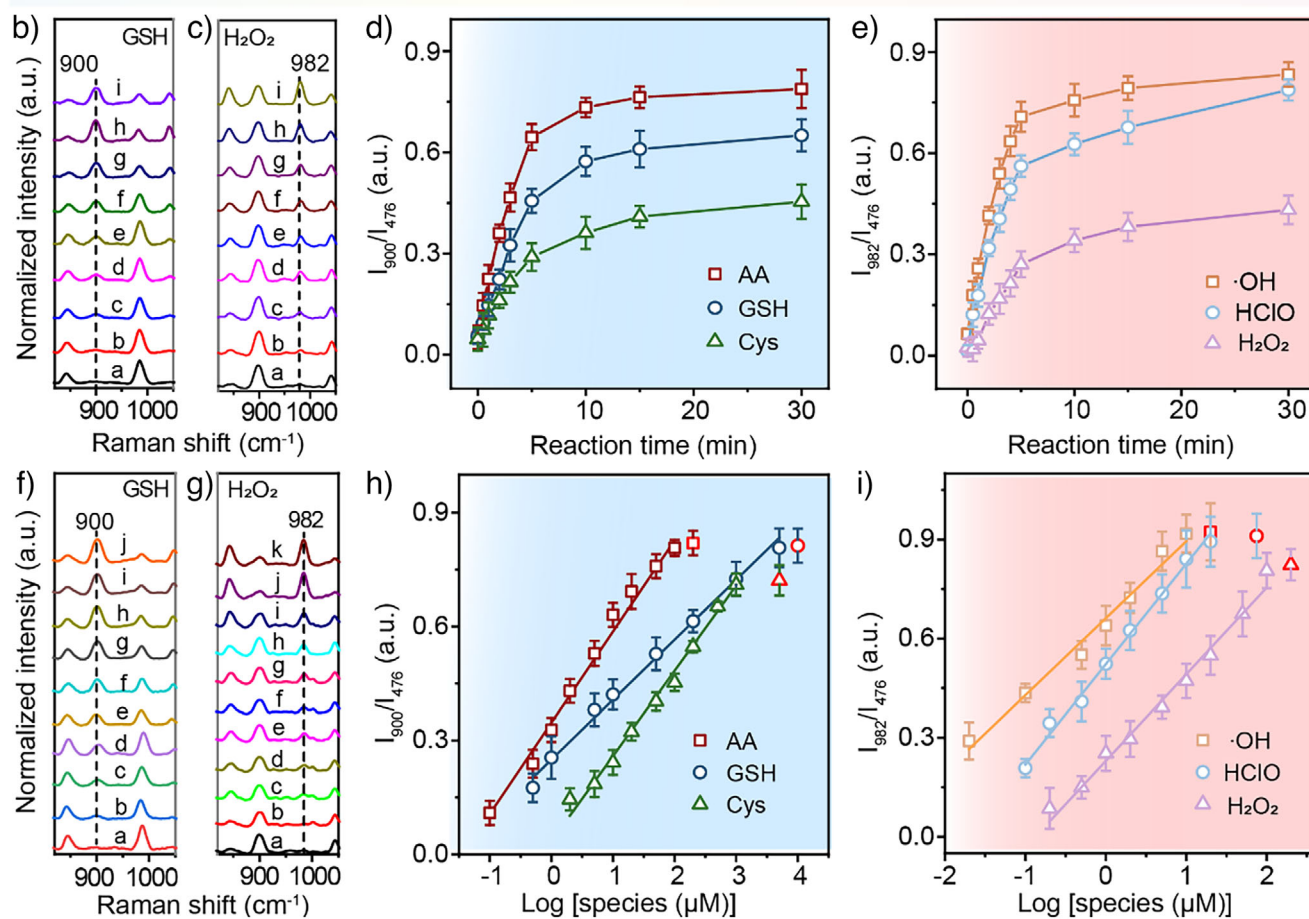
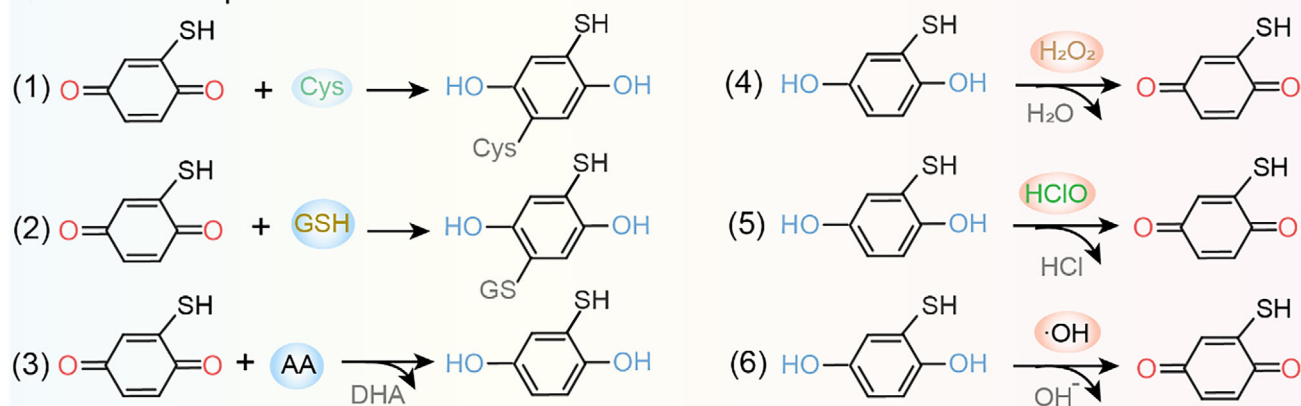


Figure 3. The investigation of redox-responsive capability of the SERS endoscope. a) The reactions between the redox-responsive probes and AA, GSH, Cys, $\cdot\text{OH}$, HClO, and H₂O₂. b) Normalized SERS spectra of the endoscope in the presence of GSH (20 μM) over time (a to i: 0, 0.5, 1, 2, 3, 5, 10, 20, and 30 min). c) Normalized SERS spectra of the endoscope in the presence of H₂O₂ (10 μM) over time (a to i: 0, 0.5, 1, 2, 3, 5, 10, 20, and 30 min). d) Plots of I_{900}/I_{476} as a function of time corresponding to AA, GSH, and Cys. e) Plots of I_{982}/I_{476} as a function of time corresponding to $\cdot\text{OH}$, HClO, and H₂O₂. f) Normalized SERS spectra of the endoscope after reacting with different concentrations of GSH (a to j: 0, 0.5, 1, 5, 10, 50, 200, 1000, 5000, 10 000 μM). g) Normalized SERS spectra of the endoscope after reacting with different concentrations of H₂O₂ (a to k: 0, 0.2, 0.5, 1, 2, 5, 10, 20, 50, 100 and 200 μM). h) Plots of I_{900}/I_{476} as a function of different species (AA, GSH, and Cys) concentrations. i) Plots of I_{982}/I_{476} as a function of different species ($\cdot\text{OH}$, HClO, and H₂O₂) concentrations. The value shown in light red represented the concentration that exceeded the upper limit of detection. Data points with error bars present the mean \pm SD of independent measurements ($n = 3$).

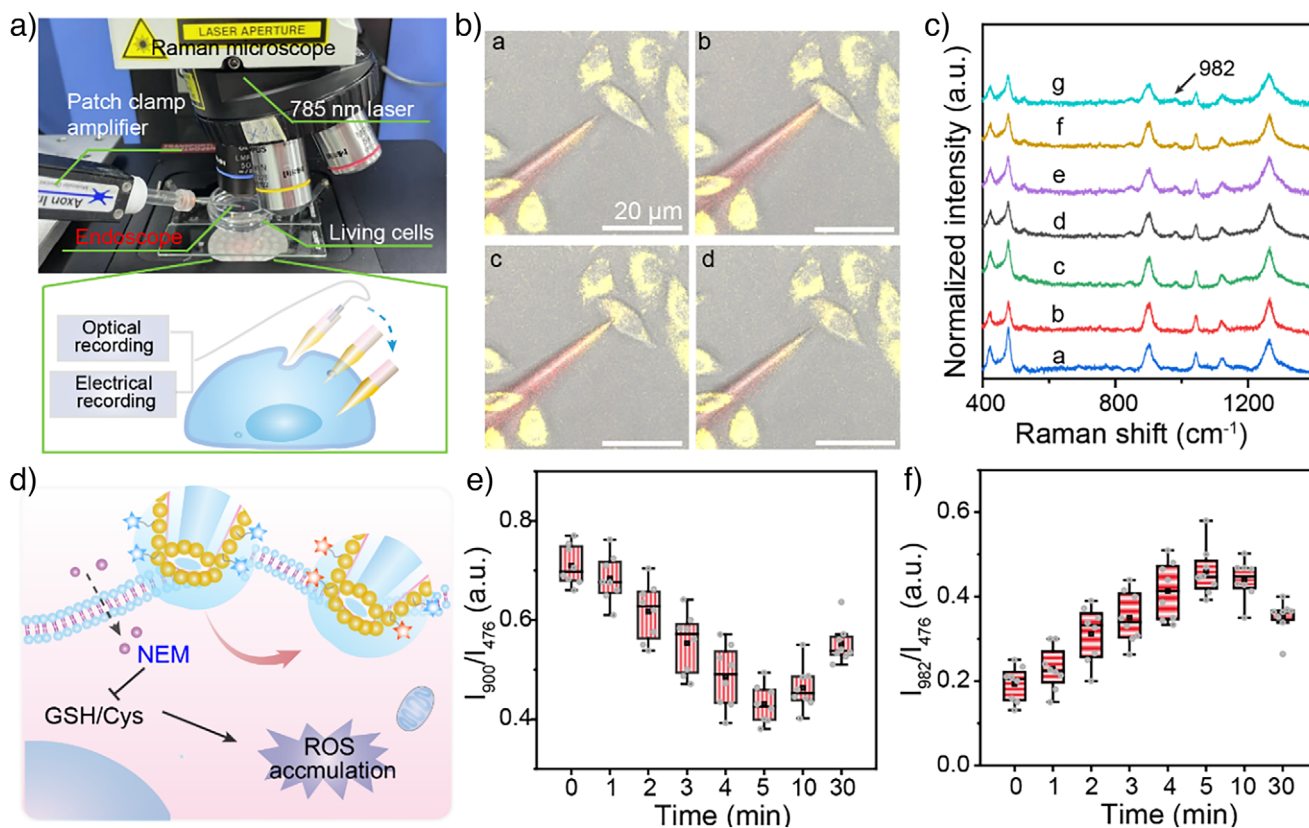


Figure 4. a) Typical picture of living cells on the mobile platform under the lens for simultaneous SERS and electrical measurements. b) The merged fluorescence images for illustrating the processes of approaching, touching, insertion, and withdrawal of the endoscope when monitoring intracellular redox metabolism. Cells were stained by rhodamine 6 G and the endoscope was loaded with Cy5. c) SERS spectra corresponding to the measurement process (a. approaching, b. touching, c. insertion, d–g. insertion for 10, 30, 60, and 90 min, respectively). d) The schematic of real-time monitoring of changes in ROS and GSH contents. Plots of e) I_{900}/I_{476} and f) I_{982}/I_{476} obtained from eight individual living cells stimulated by NME over time. The size of the endoscope was around 550 nm. Data with error bars present the mean \pm SD of independent measurements ($n = 8$). Each point represents an individual sample. Boxes represent interquartile range, line inside box denotes median.

mechanical properties of cell membrane. As shown in Figures 5b and S27, the amplitude of current and duration time reached 44.4 ± 9.75 pA and 12.5 ± 4.11 ms respectively without drugs treatment, which was attributed to the regular oscillations of cell membrane deformation.^[43,44] Erastin and (1S, 3R)-RAS-selective lethal 3 (RSL3) are two widely used ferroptosis inducers.^[45,46] In living cells, erastin affects GSH synthesis by suppressing cystine-glutamate reverse transporter (system Xc⁻) with activation of transcription factor 3 to reduce the import of cysteine, a kind of synthetic substrates of GSH (Figure 5a, pathway 1). The current amplitude decreased by nearly 30 pA under erastin stimulation, while the duration time become shorter (10.1 ± 2.74 ms, $n = 50$) (Figures 5c and S28). This can be attributed to the damage of plasma membrane elasticity caused by lipid peroxidation during ferroptosis (Figures S29 and S30). In Figure 5d,e, and S31, SERS statistical analysis showed that I_{982}/I_{476} and I_{900}/I_{476} reached to 0.41 ± 0.12 and 0.50 ± 0.10 ($n = 50$) respectively after being treated by erastin, significantly different from that of untreated cells (0.18 ± 0.07 ; 0.74 ± 0.15 , $n = 30$, Figure S32), which confirms that the brief inhibition of system Xc⁻ could lead to excessive consumption of GSH. GSH depletion further deactivated glutathione peroxidase 4

(GPX4) and increased ROS level, as evidenced by Figures S33 and S34.

Another inducer RSL3 covalently binds GPX4 and directly inhibit its activity to prevent ROS elimination (Figure 5a, pathway 2). With the treatment with RSL3, an increase of I_{982}/I_{476} to 0.34 ± 0.10 and a decrease of I_{900}/I_{476} to 0.57 ± 0.13 could be observed, implying a relatively low level of oxidative stress (Figure 5d,e, and S34). Interestingly, the RSL3 treatment resulted in an average duration time and current response (9.4 ± 2.60 ms, 21.6 ± 4.43 pA, $n = 50$) (Figures 5f and S35), indicating a low damage of the membrane integrity (Figure S30). Next, linear discriminant analysis (LDA) were used to classify three types of current signals above (Figure 5g). The signals could be well-separated by LDA at the 95% confidence interval, indicating the large difference among untreated, erastin- and RSL3-treated groups. The difference could be attributed that unlike erastin, further burst of ROS to attack the cell membrane was not allowed under RSL3 treatment without affecting cysteine uptake and GSH synthesis. The dysregulated redox metabolism with loss of plasma membrane integrity were in accordance with the previous findings.^[41,43] More remarkable ferroptosis behavior was observed by additionally using

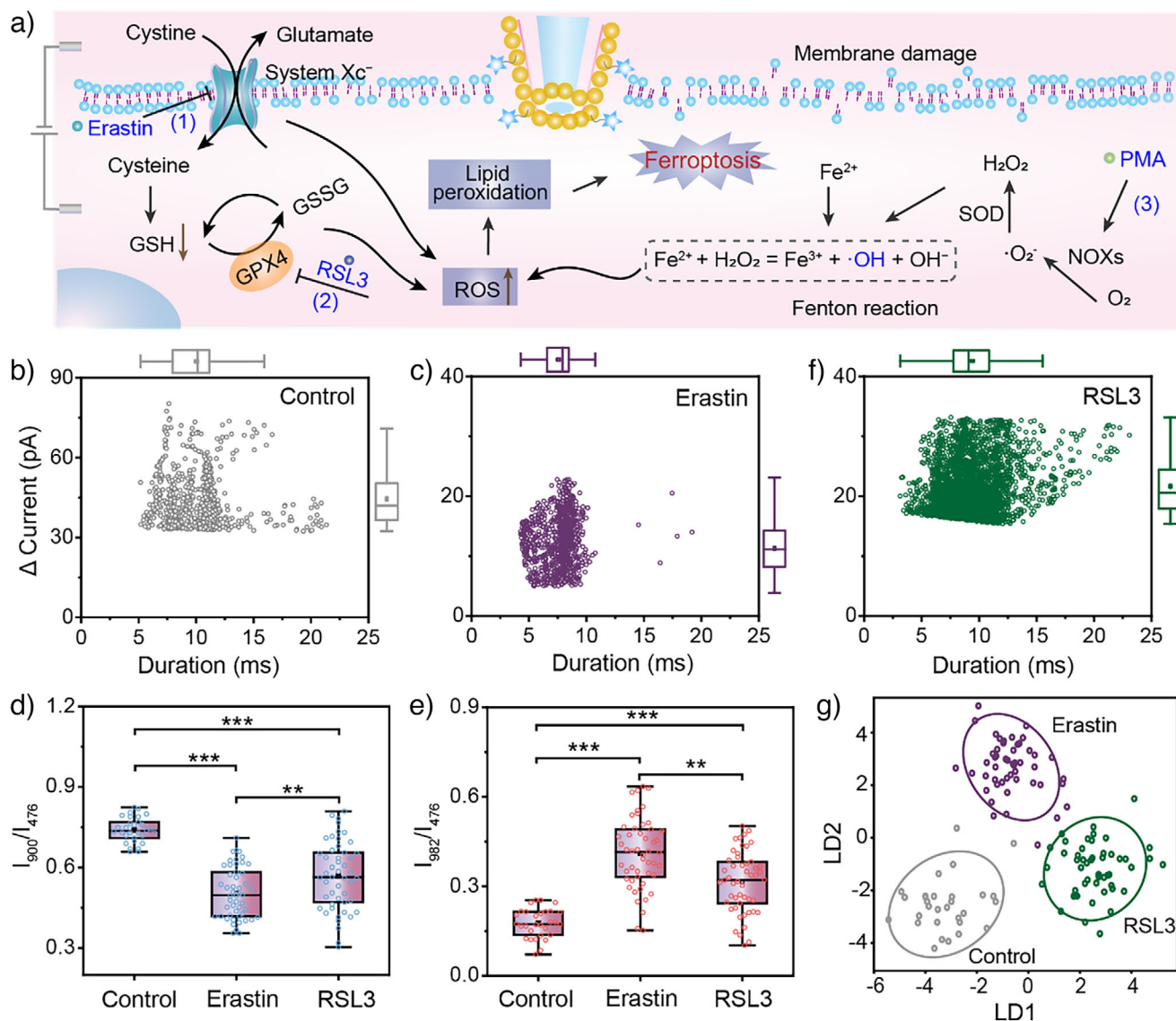


Figure 5. a) Schematic illustration of relevant mechanisms of ferroptosis induced by different drugs. Scatter and box plots for current magnitude and duration time corresponding to control group b), and erastin-treated group c). Box plots of d) I_{900}/I_{476} and e) I_{982}/I_{476} analysis corresponding to control group, erastin- and RSL3-treated group. f) Scatter and box plots for current magnitude and duration time corresponding to RSL3-treated group. g) LDA results for three types of current signals obtained from control, erastin- and RSL3-treated groups. The size of the endoscope was around 550 nm. Data with error bars present the mean \pm SD of independent measurements (Control group, $n = 30$; Treated group, $n = 50$). Each point represents an individual sample. Boxes represent interquartile range, line inside box denotes median. The probability (P) values were analyzed by Student's two-sided t test ($*p < 0.05$, $**p < 0.01$, $***p < 0.001$).

phorbol 12-myristate 13-acetate (PMA), a known ROS inducer which triggers the oxidation of oxygen by NADPH oxidase (NOX) and formation of superoxide anion ($\cdot O_2^-$) that turns into H_2O_2 under superoxide dismutase (SOD) catalysis (Figure 5a, pathway 3).^[47] Figures S36 and S37 show the current amplitude sharply decreased to 164 ± 53.8 pA with a relatively short duration time (10.2 ± 4.7 ms, $n = 30$). This was primarily because the highly toxic $\cdot OH$ that was converted from endogenous H_2O_2 by ferrous ions oxidized polyunsaturated fatty acids,^[48] resulting in the burst of lipid ROS known as “ROS-induced ROS release,” which further destroyed cellular redox homeostasis and cell membrane integrity (Figure S30). Accordingly, via simultaneous optical

and electrical recording, we can elucidate the complex interplay between redox metabolism and membrane integrity in response to underlying distinct mechanisms of different ferroptosis inducers.

Conclusion

In summary, the plasmonic NP monolayer has been successfully adopted with nanopipettes to monitor redox metabolism at the single-cell level. The method leveraged the strong enhancement from uniform hotspots created by collective plasmon resonance coupling in plasmonic monolayer,

enabling highly sensitive and reproducible SERS detection of commonly existing redox species. Combined with a high-precision nano-positioning system, it allows for real-time and in situ monitoring of dynamic redox fluctuations in single cells with high spatial resolution and minimal invasiveness. Particularly, further study of single-cell ferroptosis aided by nanopipette-based electrical measurements enhanced the endoscope's versatility to distinguish the mechanisms of various ferroptosis inducers by correlating redox metabolism changes with cell membrane integrity. The compatibility with single-cell analysis makes the endoscope a highly versatile tool, holding potential for revealing insights into the complex interplay between redox metabolism and related physiopathological conditions.

Acknowledgements

This work was financially supported by the National Natural Science Foundation of China (Grant Nos. 22304042, 22176058, 52473209, and 52222316), the Fundamental Research Funds for the Central Universities (222201717003), and the "Pioneer" and "Leading Goose" R&D Program of Zhejiang (2025C02250(SD2) and 2024C03228).

Data Availability Statement

The data that support the findings of this study are available from the corresponding author upon reasonable request.

Keywords: AuNP monolayer • Ferroptosis • Nanopipette • Redox metabolism • Single cell

- [1] J. Sun, K. Du, J. Diao, X. T. Cai, F. D. Feng, S. Wang, *Angew. Chem. Int. Ed.* **2020**, *59*, 2–9.
- [2] J. Y. Zhu, M. W. Jiang, H. Ma, H. J. Zhang, W. N. Cheng, J. Li, L. Cai, X. X. Han, B. Zhao, *Angew. Chem. Int. Ed.* **2019**, *58*, 16499–16503.
- [3] W. C. Yen, Y. H. Wu, C. C. Wu, H. R. Lin, A. Stern, S. H. Chen, J. C. Shu, D. T. Y. Chiu, *Redox Biol.* **2020**, *28*, 101363.
- [4] D. B. Cheng, X. H. Zhang, Y. J. Gao, L. Ji, D. Hou, Z. Wang, W. Xu, Z. Y. Qiao, H. Wang, *J. Am. Chem. Soc.* **2019**, *141*, 7235–7239.
- [5] C. Schubert, *Nature* **2011**, *480*, 133–137.
- [6] K. Hu, T. D. Nguyen, S. Rabasco, P. E. Oomen, A. G. Ewing, *Anal. Chem.* **2021**, *93*, 41–71.
- [7] S. Kim, J. B. Chae, D. Kim, C. W. Park, Y. Sim, H. Lee, G. Park, J. Lee, S. Hong, B. Jana, C. Kim, H. Chung, J. H. Ryu, *J. Am. Chem. Soc.* **2023**, *145*, 21991–22008.
- [8] R. Jia, M. V. T. Mirkin, *Chem. Sci.* **2020**, *11*, 9056–9066.
- [9] S. S. Anumita, E. W. Anna, A. K. Jonathan, J. R. Steven, M. H. Gary, A. B. Lane, *Chem. Sci.* **2015**, *6*, 3334.
- [10] L. Jiang, X. Wang, J. Zhou, Q. Q. Fu, B. Lv, Y. Sun, L. P. Song, Y. J. Huang, *Adv. Sci.* **2023**, *11*, 2306125.
- [11] S. E. J. Bell, G. Charron, E. Cortes, J. Kneipp, M. L. De La Chapelle, J. Langer, M. Prochazka, V. Tran, S. Schlucker, *Angew. Chem. Int. Ed.* **2020**, *59*, 5454–5462.
- [12] C. A. R. Auchinvole, P. Richardson, C. McGuinness, V. Mallikarjun, K. Donaldson, H. McNab, C. J. Campbell, *ACS Nano* **2012**, *6*, 888–896.
- [13] P. I. T. Thomson, V. L. Camus, Y. Y. Hu, C. J. Campbell, *Anal. Chem.* **2015**, *87*, 4719–4725.
- [14] S. Bonhommeau, G. S. Cooney, Y. H. Huang, *Chem. Soc. Rev.* **2022**, *51*, 2416–2430.
- [15] D. Mrdenovic, Z. X. Tang, Y. Pandey, W. T. Su, Y. Zhang, N. Kumar, R. Zenobi, *Nano Lett.* **2023**, *23*, 3939–3946.
- [16] D. Mrdenovic, W. J. Ge, N. Kumar, R. Zenobi, *Angew. Chem. Int. Ed.* **2022**, *61*, e202210288.
- [17] Y. Wang, D. D. Wang, G. H. Qi, P. Hu, E. K. Wang, Y. D. Jin, *Anal. Chem.* **2023**, *95*, 16234–16242.
- [18] V. Brasiliense, J. E. Park, Z. Chen, R. P. Van Duyn, G. C. Schatz, *J. Raman Spectrosc.* **2021**, *52*, 339–347.
- [19] Y. R. Wen, J. Liu, H. He, S. S. C. Li, Z. Liu, *Anal. Chem.* **2020**, *92*, 12498–12508.
- [20] S. Hanif, H. L. Liu, M. Chen, P. Muhammad, Y. Zhou, J. Cao, S. A. Ahmed, J. J. Xu, X. H. Xia, H. Y. Chen, K. Wang, *Anal. Chem.* **2017**, *89*, 2522–2530.
- [21] E. A. Vitol, Z. Orynbayeva, M. J. Bouchard, J. Azizkhan-Clifford, G. Friedman, Y. Gogotsi, *ACS Nano* **2009**, *3*, 3529–3536.
- [22] F. Lussier, D. Missirlis, J. P. Spatz, J. F. Masson, *ACS Nano* **2019**, *13*, 1403–1411.
- [23] X. J. Zhao, S. Campbell, G. Q. Wallace, A. Claing, C. G. Bazuin, J. F. Masson, *ACS Appl. Mater. Interfaces* **2019**, *11*, 4373–4384.
- [24] X. J. Zhao, J. S. Wang, Y. C. Jia, *Talanta* **2024**, *270*, 125608.
- [25] Y. C. Lu, P. C. Tseng, M. J. Yang, C. J. Wang, Y. C. Ling, C. F. Lin, H. Y. Hsueh, *Adv. Optical Mater.* **2023**, *11*, 2202280.
- [26] G. Q. Wallace, E. Ringe, K. Faulds, D. Graham, J. F. Masson, *Adv. Optical Mater.* **2024**, *12*, 2401640.
- [27] T. D. Nguyen, M. S. Song, N. H. Ly, S. Y. Lee, S. W. Joo, *Angew. Chem. Int. Ed.* **2019**, *58*, 2710–2714.
- [28] W. K. Wang, F. Zhao, M. Z. Li, C. P. Zhang, Y. H. Shao, Y. Tian, *Angew. Chem. Int. Ed.* **2019**, *58*, 5256–5260.
- [29] L. P. Song, X. Y. Zhu, Y. J. Huang, *Acta Polymerica Sinica* **2023**, *54*, 870–891.
- [30] M. Li, C. P. Ding, D. Zhang, W. W. Chen, Z. J. Yan, Z. K. Chen, Z. Y. Guo, L. H. Guo, Y. J. Huang, *Adv. Sci.* **2023**, *10*, 2303159.
- [31] L. P. Song, B. B. Xu, Q. Cheng, X. Y. Wang, X. N. Luo, X. Chen, T. Chen, Y. J. Huang, *Sci. Adv.* **2021**, *7*, eabk2852.
- [32] Z. L. Huang, X. Lei, Y. Liu, Z. W. Wang, X. J. Wang, Z. M. Wang, Q. H. Mao, G. W. Meng, *ACS Appl. Mater. Interfaces* **2015**, *7*, 17247–17254.
- [33] F. Lussier, T. Brulé, M. Das, T. Vishwakarma, J. P. Spatz, J. F. Masson, *Nano Lett.* **2016**, *16*, 3866–3871.
- [34] J. Song, C. H. Xu, S. Z. Huang, W. Lei, Y. F. Ruan, H. J. Lu, W. Zhao, J. J. Xu, H. Y. Chen, *Angew. Chem. Int. Ed.* **2018**, *57*, 13226–13230.
- [35] L. Jiang, Y. He, M. H. Lan, X. Ding, Q. Y. Lu, L. P. Song, Y. J. Huang, D. W. Li, *Anal. Chem.* **2024**, *96*, 7497–7505.
- [36] A. Tuzet, M. S. Rahantaniaina, G. Noctor, *Antioxid. Redox Signal.* **2019**, *30*, 1238–1268.
- [37] X. Q. Jiang, J. W. Chen, A. Bajic, C. W. Zhang, X. Z. Song, S. L. Carroll, Z. L. Cai, M. L. Tang, M. S. Xue, N. H. Cheng, C. P. Schaaf, F. Li, K. R. MacKenzie, A. C. M. Ferreone, F. Xia, M. C. Wang, M. Maletic-Savatic, J. Wang, *Nat. Commun.* **2017**, *8*, 16087.
- [38] Q. Q. Li, X. G. Ge, J. M. Ye, Z. Li, L. C. Su, Y. Wu, H. H. Yang, J. B. Song, *Angew. Chem. Int. Ed.* **2021**, *60*, 7323–7332.
- [39] B. Sreeparna, F. R. Hernan, *Nucleic Acids Res.* **2005**, *33*, 1410–1419.
- [40] H. Yan, F. Huo, Y. Yue, J. Chao, C. Yin, *J. Am. Chem. Soc.* **2021**, *143*, 318–325.
- [41] H. Bayir, S. J. Dixon, Y. Y. Tyurina, J. A. Kellum, V. E. Kagan, *Nat. Rev. Nephrol.* **2023**, *19*, 315–336.
- [42] A. Linkermann, *Nat. Cancer* **2024**, *5*, 12–13.
- [43] J. Lv, X. Y. Wang, X. Y. Zhou, D. W. Li, R. C. Qian, *Anal. Chem.* **2022**, *94*, 13860–13868.

- [44] X. Y. Wang, J. Lv, Q. Hong, Z. R. Zhou, D. W. Li, R. C. Qian, *Anal. Chem.* **2021**, *93*, 13967–13973.
- [45] W. S. Yang, R. SriRamaratnam, M. E. Welsch, K. Shimada, R. Skouta, V. S. Viswanathan, J. H. Cheah, P. A. Clemons, A. F. Shamji, C. B. Clish, L. M. Brown, A. W. Girotti, V. W. Cornish, S. L. Schreiber, B. R. Stockwell, *Cell* **2014**, *156*, 317–331.
- [46] Z. Z. Kang, J. J. Jiang, Q. Tu, S. T. Liu, Y. Zhang, D. E. Wang, J. Y. Wang, M. S. Yuan, *J. Am. Chem. Soc.* **2023**, *145*, 7, 4324.
- [47] K. Liu, Z. Zhang, R. J. Liu, J. P. Li, D. C. Jiang, R. R. Pan, *Angew. Chem. Int. Ed.* **2023**, *9*, e202303053.
- [48] Z. Y. Shen, T. Liu, Y. Li, J. Lau, Z. Yang, W. P. Fan, Z. J. Zhou, C. R. Shi, C. M. Ke, V. I. Bregadze, S. K. Mandal, Y. J. Liu, Z. H. Li, T. Xue, G. Z. Zhu, J. Munasinghe, G. Niu, A. G. Wu, X. Y. Chen, *ACS Nano* **2018**, *12*, 11355–11365.

Manuscript received: January 25, 2025

Revised manuscript received: June 19, 2025

Accepted manuscript online: June 19, 2025

Version of record online: ■ ■ ■ ■

Research Article

Single-Cell Redox Metabolism

L. Jiang, M. Zhao, H. Xu, X. Ding,
Q. Lu, J. Liu, L. Song, L. Gong, D. Li*,
Y. Huang* e202502129

Plasmonic Nanoparticle Monolayer-
Decorated Nanopipette Enabling in
Situ Monitoring of Single-Cell Redox
Metabolism

A plasmonic nanoparticle monolayer-decorated nanopipette was developed to visualize single-cell redox metabolism. Leveraging strong near-field coupling within the monolayer that forms uniform hotspots, our method enables highly sensitive and reproducible tracking of redox metabolism changes, which deepens the understanding of single-cell ferroptosis.

